ANALYSIS OF CEDBT AND CESM PERFORMANCE USING A REALISTIC X-RAY SIMULATION PLATFORM

R. Sánchez de la Rosa[*†], *A.-K. Carton*[*], *P. Milioni de Carvalho*[*], *I. Bloch*[†], *S. Muller*[*]

[*]GE Healthcare, Buc, France
[†]LTCI, Télécom ParisTech, Université Paris-Saclay, Paris, France

ABSTRACT

Contrast Enhanced Spectral Mammography (CESM) and Contrast Enhanced Digital Breast Tomosynthesis (CEDBT) are multi-energy X-ray imaging techniques involving the injection of a vascular contrast agent. Both techniques provide information on hypervascularization of lesions through contrast uptake. CESM has proved to deliver a better diagnosis of breast cancer than diagnostic mammography. CEDBT is a promising technique which provides 3D information on the contrast uptake distribution. In this paper, new steps in the image acquisition process of a previously presented image acquisition simulation platform are described, including models of scatter, image lag and electronic noise. Using this simulation platform, 290 CESM and CEDBT images were generated. A human observer experiment was then performed to compare lesion detectability and characterization. The results indicate a similar detectability and an improved characterization of shape and contrast enhancement distribution using CEDBT.

Index Terms— X-ray image chain simulation, Contrast Enhanced Spectral Mammography, Contrast Enhanced Digital Breast Tomosynthesis, detection and characterization evaluation.

1. INTRODUCTION

Contrast-Enhanced Spectral Mammography (CESM) has been proposed as a potential alternative of Contrast-Enhanced Magnetic Resonance Imaging (CE-MRI) for breast cancer diagnosis at a lower cost [1]. Both imaging techniques use a vascular contrast agent and provide both morphological and functional images of the breast, allowing for the detection of abnormal vascular development and lesion contrast uptake. In CESM, projection images are acquired at two energies and recombined to obtain iodine-equivalent images. CESM remains however a two-dimensional technique providing a 2D representation of the contrast distribution in the 3D breast. It is expected that Contrast Enhanced Digital Breast Tomosynthesis (CEDBT) may partially alleviate this limitation. Conceived as a dual-energy (DE) tomographic technique, CEDBT provides 3D reconstructed information of the injected iodinated contrast uptake.

A recent preliminary report from an ongoing clinical feasibility study has demonstrated the potential clinical value of CEDBT versus CESM in terms of lesion detectability and margins characterization [2]. In previous research [3], we also compared lesion detection and characterization performance of CESM and CEDBT in simulated images. The images were created with a platform modeling only partially the physics of the acquisition process. The realism of the acquisition simulation may however impact detection and characterization performance. In this work, we present an image acquisition platform with augmented realism, by modeling image lag, electronic noise and X-ray scatter. Finally, we performed a human observer experiment to evaluate detectability and characterization of CESM and CEDBT, using the BIRADS lexicon for CE-MRI, which describes the accepted clinically important charateristics [4].

2. SIMULATION OF X-RAY IMAGES

2.1. Image acquisition

CESM and CEDBT acquisitions were simulated using an analytical ray-tracing projector [5]. In previous work, low-energy (LE) and high-energy (HE) images were created by considering mono-energetic primary X rays and quantum noise as the only noise source. Detector blur of commercially available systems (SenoBright HD and Senographe Pristina, GE Healthcare, Chicago, IL, USA) was simulated by filtering the images with an empirically assessed convolution kernel. The photon flux was tuned to match the signal-to-noise ratio (SNR) of simulated images with real images acquired under automatic exposure mode. In this work, to increase the realism of the simulations, three new elements, based on the underlying physics and empirical data, were modeled and included into the platform: imaging lag, electronic noise and X-ray scatter of the imaged object.

Electronic noise refers to the random signal produced by the different electronic components of the detector [6]. It is additive, uncorrelated to quantum noise, detector integration time dependent, and is composed of a heterogeneous collection of noise sources (thermal noise and shot noise). The relative importance of electronic noise to the total noise increases at low exposure acquisitions such as in CEDBT [7]. The electronic noise is modeled as a random white Gaussian noise with zero mean [8]. The relationship between noise variance and detector integration time, t, is modeled as a quadratic function: $\varepsilon \sim N(0, \beta t^2)$, where β is the parameter used to fit the model to experimental measures.

The magnitude of electronic noise was experimentally assessed from acquisitions without X-ray irradiation. The electronic noise model was validated by comparing the signal intensity histograms of simulated and experimentally acquired images using the Earth Moving Distance (EMD) between histograms [9]. We found a normalized EMD inferior to 0.9% compared to the maximum possible value of EMD, for three different integration times. Considering electronic noise contribution to total noise (i.e. 12.5% of total variance in worst case scenario in our study conditions), this was judged a fair approximation.

Image lag is caused by incomplete detector read-out, resulting in a fraction of the previous projection image being carried over to the next projection images [10]. This causes a less efficient texture cancellation in iodine-recombined images that may lead to residual

signal which might be confounded with iodine uptake [11]. The nature of this phenomenon can be interpreted as a finite impulse response (FIR) filter, where signal intensity in a projection n of an acquisition sequence depends on the signal intensities in the first lag-free image and subsequent lag-containing previously acquired projections:

$$y[n] = x[n] + \sum_{k=1}^{n-1} h[k]x[n-k] \tag{1}$$

where y is a projection with lag, x a projection without lag, h the lag coefficients, and n the projection number in an acquisition sequence.

From ideally identical projections (i.e. $\forall (i,j) \in \mathbb{N}, x[i] = x[j]$), the lag coefficients can be computed from actual acquisitions as:

$$h[n] = \frac{y[n+1] - y[n]}{x[n]} \tag{2}$$

In the CEDBT acquisition sequence considered here, nine pairs of LE and HE projections are acquired, and the lag results from both types of acquisitions. The signal intensities in the nth LE projections can be estimated as:

$$
\begin{aligned}
y_{LE}[n] = x_{LE}[n] + \sum_{k=1}^{n-1} h_{LE}[2(n-k)]x_{LE}[k] + \\
\sum_{k=1}^{n-1} h_{HE}[2(n-k)-1]x_{HE}[k]
\end{aligned}
\tag{3}
$$

and a similar equation for y_{HE}.

The lag coefficients were experimentally estimated from two static DBT acquisition sequences (i.e. with tube angle at zero degree) consisting of only LE and of only HE projections. Since the magnitude of the image lag depends on the signal intensity, acquisitions were acquired at the signal intensity levels corresponding to those considered for the image simulations described in Section 3. Our model of image lag was validated using an experimentally acquired static CEDBT sequence consisting of 9 pairs of LE/HE acquisitions. Maximum error between simulated and experimentally acquired CEDBT sequences was found to be smaller than the maximum error between successive acquired CEDBT sequences. More precisely, we obtained the following values:

$$\max(|y_{LE_{sim}}^m[n] - y_{LE_{acq}}^m[n]|) = 0.4\%$$
$$\max(|y_{LE_{acq}}^i[n] - y_{LE_{acq}}^j[n]|) = 0.7\%$$
$$\max(|y_{HE_{sim}}^m[n] - y_{HE_{acq}}^m[n]|) = 0.1\%$$
$$\max(|y_{HE_{acq}}^i[n] - y_{HE_{acq}}^j[n]|) = 0.2\%$$

where sim and acq refer respectively to simulated and experimentally acquired CEDBT sequences, and i, m and j refer to independent acquisition sequences.

Scatter refers here to the deflection of primary X rays when passing through an imaged object and the deflection of light photons generated in the CsI detector scintillator [12]. In DE X-ray imaging, the scatter degrades the quality of DE recombined images by reducing the SNR and sharpness of iodine-enhancing lesions. The scatter magnitude in an uniform object of thickness T can be expressed as the multiplication of the MTF and the Fourier transform of the primary image [13]:

$$\hat{I}(\nu) = \hat{P}(\nu) \cdot (e^{-\mu T} \cdot H_G(\nu) + SPR(T) \cdot H_S(\nu, T) \cdot H_G(\nu)) \tag{4}$$

where $\hat{P}$ is Fourier transform of the primary image, H_S and H_G the MTF of the X-ray scatter in the imaged object and in the scintillator, respectively, and SPR the scatter-to-primary ratio of X rays in the imaged object.

LE and HE system MTFs, containing both the contributions from X-ray and optical scattering in the CsI scintillator, were experimentally assessed using an edge method [14]. LE and HE projection images were acquired of a 2mm thick W edge positioned on top of a 5-cm thick PMMA slab covering the imaging field of view. PMMA was used as breast equivalent material. The system MTF was then computed from the edge spread function (ESF) as follows:

$$MTF(f) = \mathcal{F}\{\frac{d}{dx}ESF(x)\} \tag{5}$$

After implementation of the scatter model in the simulation platform, the mean squared error between the system MTF in simulated and experimentally acquired images was found smaller than $5 \cdot 10^{-5}$.

2.2. Image reconstruction

Iodine-recombined CEDBT slices were reconstructed using a FBP algorithm. Traditional FBP with RamLak filter applied over recombined projections delivers poor iodine image contrast in recontructed slices [15]. We modified the filter proposed by Zhou et al. [16] for FBP in DBT, to preserve an equivalent Contrast-to-Noise Ratio (CNR) in CEDBT slices compared to CESM projections. The filter, based on a modified RamLak filter combined with a weighting window, was applied before back projecting the recombined iodine images. It enables to deliver more contrasted uptakes while reducing high frequency noise.

3. HUMAN OBSERVER EXPERIMENT

Image data set. We simulated seven breast mass types to cover all morphological mass lesion descriptors in the CE-MRI BIRADS lexicon. We used a modified version of the lesion simulation platform presented in [3]. Table 1 shows the morphological lesion characteristics and dimensions used in this study. They are based on clinical findings described in [17]. Each of the lesions was simulated with three different iodine concentrations: $0.3mg/cm^3$, $0.5mg/cm^3$, and $0.8mg/cm^3$, to provide difficult, moderate and easy detection levels. The masses were inserted in a textured 3D breast phantom [18], with 27% volumetric glandular density. To model the Breast Parenchyma Enhancement (BPE) observed in clinical images, attenuation coefficients corresponding to homogeneous mixtures of fibroglandular tissue and $0.1mg/cm^3$ iodine were assigned to the fibroglandular tissue background. In total, to evaluate characterization and detectability, 105 CESM and 105 CEDBT images with lesion and 40 CESM and 40 CEDBT images without lesion were generated.

Image simulation. The proposed X-ray simulation platform was used to simulate the images. The nominal geometry of a Senographe Pristina was modeled. Mono-energetic spectra (22keV for LE, and 34keV for HE images) were considered. The total LE and HE quantum flux for the 9 CEDBT projections was the same as for the LE and HE CESM images. Electronic noise, lag, and scatter were modeled and simulated as described in Section 2.1.

Image review. Five GE Healthcare engineers, experts in mammography imaging, participated in the human observer study. Before executing the actual study, all readers participated in a training session, where multiple examples of images with all mass-lesion

Table 1. Characteristics of lesion database used in this study.

Morphological descriptors			Maximum diameter size: 8mm
Shape	**Margin**	**Enhancement**	
Round	Sharp	Homogeneous	
		Heterogeneous	Size holes: 0.6 mm
		Rim	Thickness rim: 1.31 mm
	Indistinct	Heterogeneous	
Oval	Sharp	Homogeneous	Min axis: 5 / Max axis: 9
Irregular	Sharp	Homogeneous	
	Spiculated	Homogeneous	Spicules (Number = 40): •Length = [4.8-22.5] mm •Width = [1.6-0.2] mm
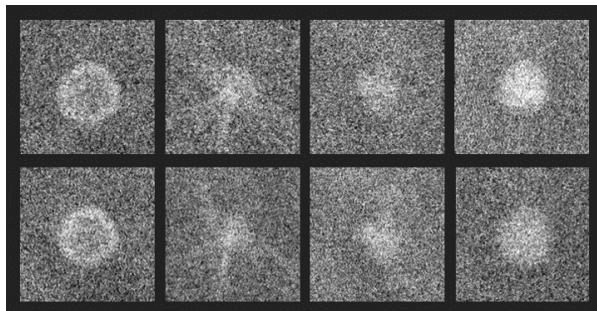
Fig. 1. Examples of simulated images. From left to right: rim, spiculated, irregular and round homogeneous lesions. On top: CESM. On bottom: CEDBT.

types and iodine concentrations as those in the actual study were presented. After training, each reader reviewed in total 57 trials. In each trial, a randomly selected iodine-recombined CESM image or a full stack of iodine-recombined CEDBT slices was presented (see examples in Figure 1). Between two trials a uniform image was presented, to reduce bias between consecutive trials. The reader was asked to answer the following questionnaire for each trial:

Q1: Is there a lesion? (Yes / No)
Q2: What is the shape of the mass? (Round / Oval / Irregular)
Q3: How can you describe its margins? (Circumscribed / Indistinct / Spiculated)
Q4: How can you describe the distribution of its contrast enhancement? (Homogeneous / Heterogeneous / Rim)
For all questions: What is your confidence level? (1-4)

We used a 4-level confidence rating: not confident at all (1), not confident (2), confident (3), very confident (4). The readers had no time limitation to answer the questionnaire.

Data analysis. The software platform iMRMC proposed by the FDA [19] was used to compute detectability and characterization ROC curves, as well as their areas under the curves (AUC). The statistical significance of the difference in the AUCs for CESM and CEDBT was estimated with the Dorfman-Berbaum-Metz (DBM) method for multi-reader ROC analysis [20] at 0.05 significance level. Fleiss' kappa coefficient was also computed to measure the agreement between reader responses.

4. RESULTS

Pooled over all readers and mass lesion types, the lesion detectability was found similar for CESM and CEDBT ($p\text{-}value = 0.52$) (Figure 2). The characterization of margins was found similar for both modalities. CEDBT outperforms CESM for shape characterization,
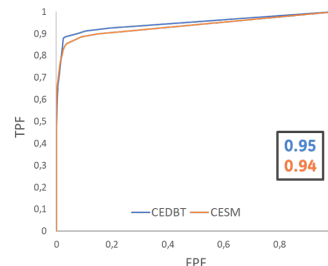
Fig. 2. Detectability ROC curve based on the answers of five readers over the ensemble of simulated images for CEDBT and CESM.
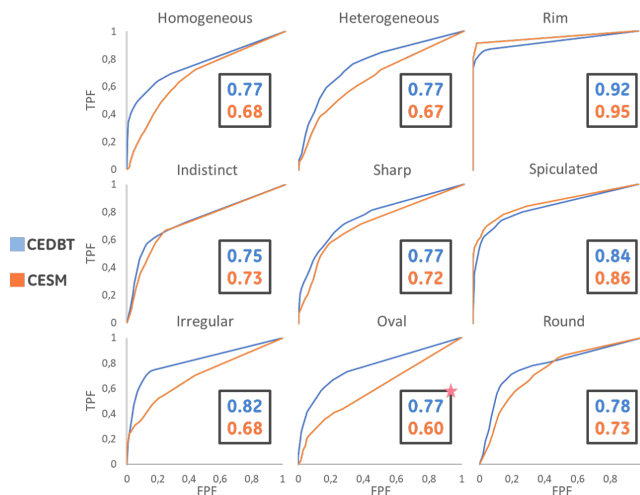
Fig. 3. Characterization ROC curves of the five readers, and corresponding AUCs, for CEDBT and CESM. From top to bottom: contrast enhancement distribution, margin, and shape descriptors. Significant difference are indicated by ★ ($\alpha = 0.05$).

and a significant difference was found for oval masses ($p\text{-}value < 0.01$). For contrast enhancement descriptors, the rim characterization was found similar for both modalities, although homogeneous and heterogeneous distributions were slightly better characterized in CEDBT (Figure 3). We also noticed that one reader, compared to the other four readers, underperformed in the characterization of spiculated masses for CEDBT (reader AUCs equal to 0.65 and 0.86 compared to the total pooled AUCs 0.84 and 0.86, for CEDBT and CESM respectively). Without considering this reader, the spiculated AUC for CEDBT increases to 0.88. However, the AUCs are still non-significantly different.

The inter-reader agreement pooled over all five readers was similar for CESM and CEDBT, for all the three mass-lesion descriptors considered. The highest response consensus was found for enhancement pattern and the lowest one for margin type (Table 2).

5. DISCUSSION AND CONCLUSION

The characterization of shape and enhancement patterns of breast masses was found better for CEDBT reconstructed slices than for CESM images. This can be explained by the fact that CEDBT dis-

Table 2. Fleiss' kappa coefficient for each descriptor and modality and its respective confidence interval ($p\text{-}value = 0.05$).

	Shape	Margin	Enhancement
CESM	0.40[0.38-0.42]	0.34[0.32-0.35]	0.59[0.58-0.61]
CEDBT	0.42[0.40-0.43]	0.32[0.30-0.33]	0.57[0.56-0.59]

tributes the 3D information into multiple planes. The characterization of lesion margins was found similar for CESM and CEDBT. We presume that this can be attributed to the presence of off-focal artifacts in the reconstructed slices.

With respect to our previous work, three main conclusions can be highlighted. First, in this work, characterization of shape and contrast enhancement was found much better for CEDBT compared to CESM. This may be due to the fact that the reviewers had access to the full stack of CEDBT slices in this study, which is close to clinical image review conditions, while in previous study only the central CEDBT slice was presented. Secondly, in our previous study, lesion detectability was found very low for CEDBT. As a consequence, only few meaningful data was available on lesion characterization performance. Also, in this previous work, poor CEDBT lesion detectability resulted from the choice of the iterative reconstruction algorithm, not optimized for CEDBT. In current work, the proposed FBP reconstruction algorithm preserves a similar detectability level for CESM and CEDBT. Finally, the weighting function introduced in our FBP filter reduces spatial resolution, which can explain the reduced margin characterization compared to our previous study.

Even if we increased the realism in our simulation platform, some phenomena were not included, such as heel effect, focal spot size and shape, and patient's movement. The impact of these effects remains for further investigation. We used a reconstruction FBP filter to match the CNR between CESM and CEDBT images. However, the recombination of LE and HE images delivers an MTF of the DE recombined image where some frequencies are attenuated [21]. Future work will include reconstruction techniques able to reduce this effect. Finally, the detectability and characterization tasks were performed using a simulation framework. As a future work, the clinical results anticipated thanks to the proposed simulation platform should be compared to true clinical evaluations when a real system will be available.

6. REFERENCES

[1] E. M. Fallenberg, F. F. Schmitzberger et al., "Contrast-enhanced spectral mammography vs. mammography and MRI – clinical performance in a multi-reader evaluation," *European Radiology*, vol. 27, no. 7, pp. 2752–2764, 2017.

[2] H. Huang, D. A. Scaduto et al., "Lesion assessment and radiation dose in contrast-enhanced digital breast tomosynthesis," in *14th International Workshop on Breast Imaging*, 2018, vol. 10718, p. 107181J.

[3] R. Sanchez De La Rosa, A. K. Carton et al., "Preliminary study of CEDBT and CESM performances using simulated analytical contrast uptakes," in *International Symposium on Biomedical Imaging*, 2018, pp. 792–795.

[4] C. D'Orsi, E. Sickles et al., *ACR BI-RADS Atlas: Breast Imaging Reporting and Data System*, American College of Radiology, Reston, VA, 2013.

[5] P. Milioni de Carvalho, *Low-Dose 3D Quantitative Vascular X-ray Imaging of the Breast*, Ph.D. thesis, Université Paris Sud-Paris XI, 2014.

[6] J. H. Siewerdsen, L. E. Antonuk et al., "Empirical and theoretical investigation of the noise performance of indirect detection, active matrix flat-panel imagers (AMFPIs) for diagnostic radiology," *Medical Physics*, vol. 24, no. 1, pp. 71–89, 1997.

[7] W. Zhao, W. G. Ji et al., "Imaging performance of amorphous selenium based flat-panel detectors for digital mammography: Characterization of a small area prototype detector," *Medical Physics*, vol. 30, no. 2, pp. 254–263, 2003.

[8] X. Gong, S. J. Glick et al., "A computer simulation study comparing lesion detection accuracy with digital mammography, breast tomosynthesis, and cone-beam CT breast imaging.," *Medical Physics*, vol. 33, no. 4, pp. 1041–1052, 2006.

[9] Y. Rubner, C. Tomasi et al., "The Earth Mover's Distance as a Metric for Image Retrieval," *International Journal of Computer Vision*, vol. 40, no. 2, pp. 99–121, 2000.

[10] J. H. Siewerdsen and D. A. Jaffray, "A ghost story: Spatio-temporal response characteristics of an indirect- detection flat-panel imager," *Medical Physics*, vol. 26, no. 8, pp. 1624–1641, 1999.

[11] A.-K. Carton, S. Puong et al., "Effects of image lag and scatter for dual-energy contrast-enhanced digital breast tomosynthesis using a CsI flat-panel based system," in *Medical Imaging: Physics of Medical Imaging*, 2011, vol. 7961, p. 79611D.

[12] J. M. Boone and V. N. Cooper, "Scatter/primary in mammography: Monte Carlo validation," *Medical Physics*, vol. 27, no. 8, pp. 1818–1831, 2000.

[13] O. Diaz, D. R. Dance et al., "Estimation of scattered radiation in digital breast tomosynthesis," *Physics in Medicine and Biology*, vol. 59, no. 15, pp. 4375–4390, 2014.

[14] A.-K. Carton, D. Vandenbroucke et al., "Validation of MTF measurement for digital mammography quality control," vol. 32, no. 6, pp. 1684–1695, 2005.

[15] D. A. Scaduto, Y.-h. Hu et al., "Dependence of contrast-enhanced lesion detection in contrast-enhanced digital breast tomosynthesis on imaging chain design," 2016, vol. 9699, pp. 136–144.

[16] J. Zhou, B. Zhao et al., "A computer simulation platform for the optimization of a breast tomosynthesis system," *Medical Physics*, vol. 34, no. 3, pp. 1098–1109, 2007.

[17] C. Dromain, *Optimisation de l'angiomammographie et de l'angiotomosynthèse double-énergie*, Ph.D. thesis, Université Paris Sud-Paris XI, 2015.

[18] Z. Li, *Task-based optimization of 3D breast x-ray imaging using mathematical observers*, Ph.D. thesis, Paris Saclay, 2017.

[19] B. D. Gallas, A. Bandos et al., "A framework for random-effects ROC analysis: biases with the bootstrap and other variance estimators," *Communications in Statistics - Theory and Methods*, vol. 38, no. 15, pp. 2586–2603, 2009.

[20] S. L. Hillis, K. S. Berbaum et al., "Recent developments in the Dorfman-Berbaum-Metz procedure for multireader ROC study analysis," *Academic Radiology*, vol. 15, no. 5, pp. 647–661, 2008.

[21] S. Richard and J. H. Siewerdsen, "Cascaded systems analysis of noise reduction algorithms in dual-energy imaging," *Medical Physics*, vol. 35, no. 2, pp. 586–601, 2008.